

# Flatness-based open-loop and closed-loop control for electrostatic quasi-static microscanners using jerk-limited trajectory design

Richard Schroedter<sup>a,\*</sup>, Matthias Roth<sup>b</sup>, Klaus Janschek<sup>b</sup>, Thilo Sandner<sup>a</sup>

<sup>a</sup>Fraunhofer Institute for Photonic Microsystems, Active Microscanner Systems, Maria-Reiche-Str.2, 01109 Dresden, Germany

<sup>b</sup>Institute of Automation, Faculty of Electrical and Computer Engineering, Technische Universität Dresden, 01062 Dresden, Germany

## Abstract

This paper describes the open-loop and closed-loop control for quasi-static microscanners exploiting the inherent flatness property. The developed nonlinear control method is verified on a gimbaled quasi-static/resonant scanning micro mirror with electrostatic staggered vertical comb (SVC) drive actuation. Based on a mechatronic micro mirror model, we present a flatness-based feed forward control method using jerk-limited trajectories to reduce undesired oscillations. For the closed-loop control we introduce a stabilizing linearizing feedback including an extended Luenberger observer for improvement of the command tracking in presence of model inaccuracies. The experimental results for both scenarios, open-loop and closed-loop control, are compared with simulations and further assessed in terms of performance and feasibility for industrial application.

**Keywords:** MEMS, quasi-static/resonant microscanner, electrostatic staggered vertical comb, jerk-limited triangle trajectory, flatness-based open-loop and closed-loop control, global extended Luenberger observer

## 1. Introduction

Quasi-static microscanners are micro-opto-electro-mechanical systems (MOEMS) [1, 2], that can perform high dynamic and precise beam positioning for various applications such as 1D/2D light detection and ranging (LIDAR) [3], medical endoscopes [4, 5], tunable laser spectrometer [6], laser projection [7, 8], bar code reading [9], or micro displays [10–12]. The advantage of these micro scanning mirrors (MSMs) is their small size and high-speed deflection in fast scanning devices. This is characterized with a high repeatability, low power consumption and mechanical reliability, due to the gimbaled mirror and the electrostatic comb drive fabricated with mono-crystalline silicon in comparison to conventional galvanometer scanners, e.g. [13]. The low mass and small dimensions show high potentials in compact devices.

In recent years fabrication and control of MEMS scanner became a more and more important issue [14, 15]. In most concepts the electrostatic forces are used as parallel-plate actuator [16–18], side-wall electrodes [19, 20] and staggered or angular vertical combs drives [21–26]. Other principles are magnetic [27, 28], thermal [29, 30] or piezoelectric [31, 32] drives.

Resonant scanning systems with restriction to sinusoidal or Lissajous scanning, as presented in [33], are state of the art. In contrast, the presented microscanner is provided with a novel *staggered vertical comb* (SVC) drive in one axis, that describes a so called *quasi-static* motion [34]. It

is capable holding a static position, tracking an arbitrary motion or oscillating in resonant mode. In contrast to parallel-plate actuators the presented SVC actuator has no *pull-in* in the respective deflection angle.

The microscanner dynamics is characterized by inherent nonlinear transducer characteristics and extremely low damped spring-mass dynamics that excites unfavorable oscillation at the mirror's eigenfrequency. Previous model-based design work has resulted in principle models for the microscanner [35–37] and open-loop control approaches including resistive impedance feedback [38], command shaping [38, 39] and optimized command trajectories [40].

The feedback control presented in this paper significantly improves the performance and control accuracy compared to the open-loop strategies demonstrated in [35, 36, 38–40] as compared in [40]. Linear methods, like [39], suffer from the representation of the inherent nonlinearities of the electrostatic comb drive and the progressive stiffness of the micro mirror's torsional spring. Referring to [37] the controller is optimized, since the acceleration, not the voltage directly, is controlled with the feedback. Furthermore we give a simple description for jerk-limited triangle trajectories with Tab. 2. The flatness-based control concept using exact linearization is a well-established method, described by [41, 42] based on the exact linearization theory [43]. Its feasibility is shown with simulations for MEMS mirrors in parallel-plate configuration in [18, 44–48], but the experimental realization is missing. This paper shows the practical feasibility of the flatness-based control concept focusing on triangle shaped trajectories required for scanning applications.

\*Corresponding author: richard.schroedter@ipms.fraunhofer.de

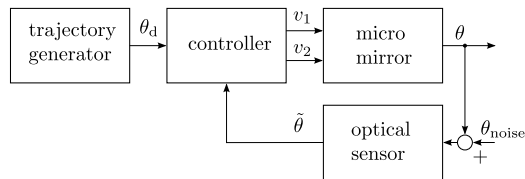


Figure 1: Control principle for the quasi-static micro mirror

In this paper, we present a comprehensive system modeling and control design for a flatness-based open-loop and closed-loop control of the quasi-static mirror axis together with the experimental results realized on a real-time system using optical sensor feedback.

We investigate an advanced trajectory design, which considers the inherent unidirectional actuation principle of the electrostatic drive, applied for triangle shaped trajectories. We proof the performance benefit compared to open-loop control of factor 4 to 18 for the flatness-based closed-loop control with experimental results using optical feedback. Finally, we discuss the influence of the harmonics of the command trajectory stimulating the mirror's resonant frequency.

Figure 1 shows the principal control structure. The trajectory generator block provides the desired trajectory with the desired scan profile and the controller block describes the observation of the mirror states from the measured position signal as well as the control output generation using the parametrized mirror model. The other blocks represent the micro mirror and the optical sensing setup for the mirror's position measurement.

The paper is organized as follows: In section 2, we are introducing the gimbaled quasi-static resonant microscanner in its applied context. Physical modeling including a reduced mechatronic system model and its simulative and experimental parameter identification is presented in section 3. In section 4, we introduce a model-based trajectory design for a typical repetitive triangle shaped trajectory using jerk limitation. Due the physical constraints we exploit the design method considering the electrostatic actuators intrinsic unidirectional torque generation and providing a reserve for closed-loop control. section 5 presents the derivation of the flatness-based open-loop and closed-loop control design. In section 6, we validate experimentally the given control concept with a real micro mirror. The performance evaluation of the experimental results will be evaluated in section 7. Finally, a summary and outlook is given in section 8.

## 2. Gimbaled quasi-static resonant microscanner

The presented gimbaled quasi-static resonant 2D microscanner, manufactured at Fraunhofer Institute for Photonics Microsystems (IPMS), cf. Fig. 2, was designed with the objective to build a 3D time-of-flight laser camera

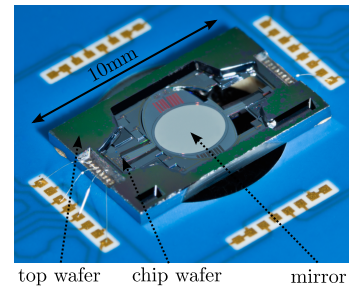


Figure 2: Photograph of tilted quasi-static/resonant 2D microscanner

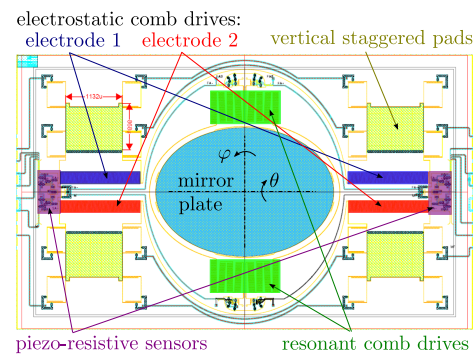


Figure 3: Layout of quasi-static/resonant 2D microscanner

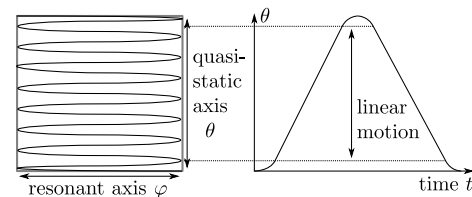


Figure 4: Typical 2D raster scanning figure combining resonant triangle shaped motion

with foveated imaging properties for robotic applications [49–52].

Fabricated in a CMOS compatible and mass production suitable fabrication process using mono-crystalline silicon, the micro mirror is a highly robust and reliable MEMS device withstanding shock accelerations above 2500 g [3].

The mirror plate has an elliptic aperture of  $2.6 \times 3.6 \text{ mm}^2$  and is gimbaled with two orthogonal axes, cf. Fig. 3, to achieve the typically required 2D scanning figure, cf. Fig. 4. The inner axis has an electrostatic *in-plane* comb drive and therefore operates in resonant mode with an eigenfrequency at 1600 Hz and a mechanical scan angle of  $\pm 20^\circ$ . The outer axis has an *out-of-plane* SVC drive [8], which allows static as well as dynamic operation up to the eigenfrequency of

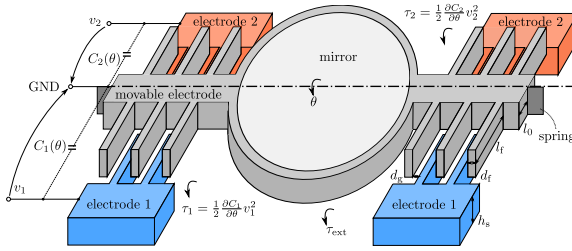


Figure 5: Staggered vertical comb (SVC) principle with electrical connections and torques (dimensions are not to scale)

120 Hz with mechanical deflections of  $\pm 10^\circ$ . The precision in wafer fabrication of less than 50 nm and the tenfold difference of both axis eigenfrequencies prevents coupling and guarantees the independent motion with a full optical scan range of  $40^\circ \times 80^\circ$ .

While the resonant axis has simple beam springs like in [53], the springs of the quasi-static axis are multiple parallel beam springs [54], to transfer parallel electric signals of the intrinsic piezo-resistive sensors and to power the comb drives of the inner axis.

The nonlinear progressive stiffness of the beam spring profile, as well as the electrostatic comb drives providing nonlinearities, are one reason for the proposed flatness-based control strategy presented in the next sections.

In this paper we focus on the quasi-static axis, even though the mirror can perform 2D scanning, because the resonant axis disturbs the optical PSD measurement, needed for the control feedback of the quasi-static axis. Experimental results of the resonant axis have been published in [49].

Both mirror axes are equipped with position sensors based on the intrinsic piezo-resistivity [55, 56] using a Wheatstone bridge circuit, that are intended to replace the optical feedback. First successful control results are shown in [57, 58].

### 3. Physical modeling

In the following section we derive the physical modeling of the quasi-static axis of the presented micro mirror including the electrostatic comb drive actuator and we introduce the relevant parameters for a model-based control.

#### 3.1. Mechatronic system model

The outer mirror frame forms a movable structure, which is located between the quasi-static comb drives and suspended with parallel torsional springs. We assume a rigid mirror plate without deformation in the quasi-static axis. Figure 5 illustrates the mechanical structure of the mirror, the comb drives and the electrical connection of the electrodes.

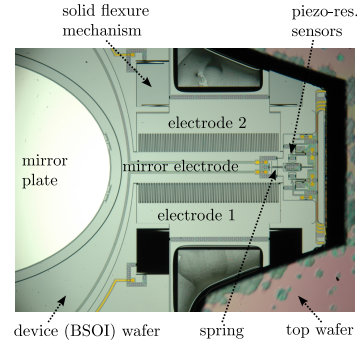


Figure 6: Detailed photograph of the staggered vertical comb drive

**Electrostatic comb drive.** The electrostatic drives are electrically isolated comb structures, which build a capacitance between the mirror electrode and the respective drive electrodes for positive and negative deflection. Figure 6 shows a photograph of the electrostatic SVC drive of one mirror side. In difference to the combs of the inner resonant axis, the fixed quasi-static combs are in a vertically staggered arrangement, cf. Fig. 5 and Fig. 7. In contrast to other known methods [21, 22, 25, 59, 60], the presented SVC is realized with a top wafer, that pushes down a solid flexure mechanism about once the substrate height of  $75 \mu\text{m}$ , as described in [61]. The comb parameter are specified in Tab. 1 according to Fig. 5.

Table 1: Specific parameter for quasi-static SVC comb drive of the presented mirror

Number of fingers per electrode $n_f$	170
Substrate height $h_s$	$75 \mu\text{m}$
Finger length $l_f$	$210 \mu\text{m}$
Finger width $d_f$	$5 \mu\text{m}$
Distance to rotation axis $l_0$	$180 \mu\text{m}$
Electrode gap $d_g$	$5 \mu\text{m}$

When applying a voltage between electrode 1 and the movable mirror electrode, the electrostatic forces lead to a tilt of the mirror with positive angle  $\theta > 0$ , and in negative direction between electrode 2 and the mirror electrode. The lateral electrostatic force between the movable electrode fingers and the mirrors fixation by the spring defines the finger stability towards a planar rotation and the mechanic contact of the fingers. The maximum stabilization voltage has been determined at  $v_{\text{max}} = 150 \text{ V}$  considering the structural finger stiffness [8].

As will derived hereafter, the ability of the comb drive to generate torque is proportional to the change in capacitance with respect to the angular deflection. Instead of measuring directly the capacitance-deflection characteristic e.g. with

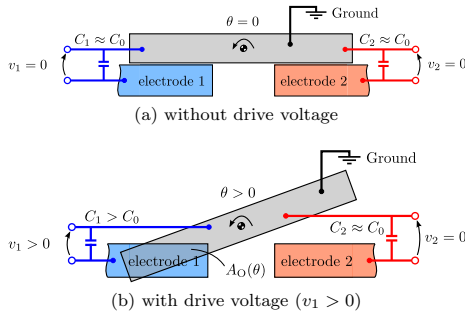


Figure 7: Illustration of the electrostatic comb drive actuation principle with the movable electrode of the tilting mirror plate (gray) and both fixed electrodes (blue and red) from side view: (a) without voltage and (b) with voltage

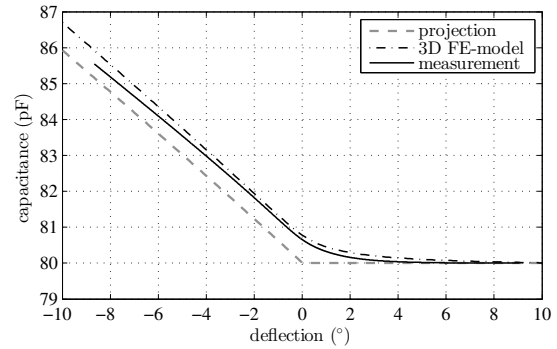
an impedance analyzer, which is depicted with inaccuracies due to the unknown electric circuit between the electrodes comprising all wires and stray capacitances for the very small capacitances, we derive the capacitance change as described in section 3.2 from the static voltage-deflection curve with Eq. (9), cf. Fig. 8 (measurement). To verify this method, we provide a projection method and a 3D finite element (FE) analysis as shown in Fig. 8. The projection curve is determined with a FE calculation in MATLAB of the overlap area  $A_O(\theta)$  for the comb electrodes (cf. Fig. 7b) using Eq. (1).

$$C'(\theta) = 2n_f \frac{\varepsilon}{d_g} A_O(\theta) \quad (1)$$

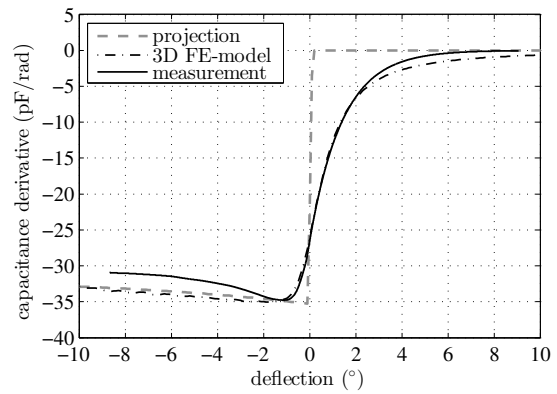
The capacitances change only in their respective angle hemisphere. In other words, if the comb fingers of a drive side do not overlap, the capacitance does not change when neglecting stray capacitances. At zero angle, the projection equals to analytic methods ([8, 25, 62, 63]) with  $A_O(0) = l_0 l_f + \frac{1}{2} l_f^2$ , resulting to  $C'(0) = 36 \text{ pF/rad}$  with Eq. (1) using the comb parameter from Tab. 1 and the permittivity for air  $\varepsilon = 8.859419 \times 10^{-12} \text{ As/(Vm)}$ . The 3D FE method computation (cf. [64]) considering stray capacitances shows an exponential decrease of the capacitance change for the emerged comb in Fig. 8a. Furthermore the constant static capacitance is determined as  $C_0 = 80 \text{ pF}$ . Nevertheless, both simulative capacitance models would lead to incorrect static deflection angles, when applying to the micro mirror.

As described before, the electrostatic comb drive acts against the torque of a nonlinear spring with  $\tau_s(\theta)$  and a small viscous damping torque  $\tau_D$ . Exploiting this relation, we propose a novel method to identify the essential change in capacitance in section 3.2.

**Mechatronic transducer model.** Our conceptual model of the mechatronic transducer is displayed in Fig. 9. With the fundamental electrostatic constitutive transducer equation  $q = C(\theta)v$  for the electrostatic transducer [65], we derive



(a) Capacitance  $C_2(\theta)$  with  $C_0 = 80 \text{ pF}$



(b) Capacitance derivative  $C'_2(\theta)$

Figure 8: Capacitance characteristic for electrode 2

the displacement current Eq. (2) for both combs:

$$i_n = \frac{dq_n}{dt} = C_n(\theta)\dot{v}_n + C'(\theta)\dot{\theta}v_n, \quad n = 1, 2. \quad (2)$$

**Lagrange formalism.** Using the Lagrange formalism of second kind [65, 66], we get Eq. (3) for the *generalized* coordinate  $\theta$  with the potential energy  $V$ , the generalized kinetic co-energy  $T^*$ , the dissipative load  $\tau_D$  and the external load  $\tau_{\text{ext}}$ :

$$\frac{d}{dt} \frac{\partial L(\theta, \dot{\theta})}{\partial \dot{\theta}} - \frac{\partial L(\theta, \dot{\theta})}{\partial \theta} = \tau_{\text{ext}} - \tau_D \quad (3a)$$

$$\text{with } L = T^*(\dot{\theta}) - V(\theta). \quad (3b)$$

The potential energy stored in the mechatronic transducer is composed of the energy stored in the spring<sup>1</sup> and in the

<sup>1</sup>The potential energy of the conservative spring torque  $\tau_s(\theta)$  is obtained by integrating the spring torque to from a point  $P$  to the reference point  $P_0$ :  $V(\theta) = \int_{P_0}^P \tau_s(\bar{\theta}) d\bar{\theta} = - \int_P^{P_0} \tau_s(\bar{\theta}) d\bar{\theta}$ . We define  $P_0 = 0$ , where the spring is not deformed and  $P = \theta$ .



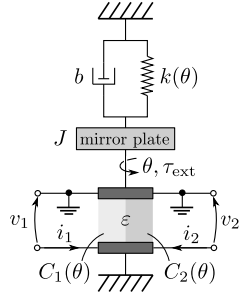


Figure 9: Schematic of the mechanically loaded generic mechatronic transducer, cf. [65]

drive capacitances, considering  $V = \int q dv$ , as follows [65]:

$$V(\theta) = \frac{1}{2}C_1(\theta)v_1^2 + \frac{1}{2}C_2(\theta)v_2^2 - \int_0^\theta \tau_s(\tilde{\theta})d\tilde{\theta}. \quad (4)$$

The kinetic co-energy is proportional to the mirror plate's moment of inertia  $J$ , the dissipative load originates from friction with the surrounding air depicted by the friction coefficient  $b$ :

$$T^* = \frac{1}{2}J\dot{\theta}^2, \quad \tau_D = b\dot{\theta}. \quad (5)$$

Using Eq. (4) and (5) the Lagrange formalism Eq. (3) yields the differential equation of the mechatronic transducer, where the torques of both combs are defined as  $\tau_1$  and  $\tau_2$ :

$$J\ddot{\theta} + b\dot{\theta} + \tau_s(\theta) = \underbrace{\frac{1}{2}C'_1(\theta)v_1^2}_{\tau_1(\theta, v_1)} + \underbrace{\frac{1}{2}C'_2(\theta)v_2^2}_{\tau_2(\theta, v_2)} + \tau_{ext} \quad (6a)$$

$$\text{with } C'_n(\theta) = \frac{dC_n(\theta)}{d\theta}, \quad n = 1, 2. \quad (6b)$$

Equation (6) represents a damped spring-mass oscillator with nonlinear behavior for spring and drive input.

*Unidirectional actuation.* As mentioned before, it is important to realize that, depending on the sign of the deflection, only one of the electrostatic combs may generate a substantial electrostatic torque, because the respectively opposite comb is emerged. This is illustrated by the capacitance curves in Fig. 8 (projection). Moreover, the attractive electrostatic torque between the mirror plate and the respective drive electrode is restricted to being unidirectional. This means, the mirror combs can only pull but not push the mirror. The unidirectional nature of the electrostatic torques has a significant effect on the control design later in section 5, that leads us to introduce a *comb switch*. In addition, this restriction is considered in the trajectory design in section 4.2.

*Impedance feedback.* Due to fundamental electromechanical conversion of energy in the mechatronic transducer electrical impedance feedback can significantly enlarge the system damping. In [35] we have investigated the damping-optimal resistance of  $15M\Omega$ , that significantly reduces undesired oscillation for single-sided actuation with one comb drive. However, when switching between the comb drives, we discovered an overdamping of the peak current (cf. Eq. (2)) near zero deflection, caused by the nonlinear transducer property Eq. (6). As consequence, unfavorable oscillation was observed again. Variable resistances may be a solution to apply beneficial impedance feedback.

### 3.2. Parameter identification

After deriving the model, the next step consists in identifying the model parameter of the investigated mechatronic system. Let us start with the mechanical part, the left side of Eq. (6). The mirror inertia including the mirror frame has been determined at  $J = 3.89 \times 10^{-12} \text{ kgm}^2$  with a finite element model using ANSYS®. Due to the geometric tolerance of 50 nm for the MEMS fabrication process, the uncertainty for the mirror inertia is about 0.15 %. Different damping effects for tiltable plates with comb drive based on Couette and Poiseuille flow have been analyzed in [8, 67]. The system's damping behavior has been shown predominately linear in decay curve experiments [39]. Therefore, we propose a linear viscous damping model that fits well to the measured decay characteristic shown in Fig. 13. Solid body damping in the springs can be neglected since they are of mono-crystalline silicon. The finite element simulation of the nonlinear progressive spring shows a quadratic stiffness characteristic (discussed in [68]), known for Duffing oscillators [69, 70], see Fig. 10. The nonlinear spring moment follows with Eq. (7).

$$\tau_s(\theta) = \int_0^\theta k(\tilde{\theta})d\tilde{\theta}, \quad k(\theta) = k_0 + k_2\theta^2 \quad (7)$$

After an impulse excitation evaluate the decay curve for small deflections ( $\hat{\theta}_0 < 0.1^\circ$ ) using the decaying sinusoidal oscillation function Eq. (8) with a least-square approximation starting at the maximum  $\hat{\theta}_0$  [70, 71].

$$\sum_i \left[ \theta(t_i) - \hat{\theta}_0 e^{-D\omega_0 t_i} \cos\left(\sqrt{1 - D^2}\omega_0 t_i\right) \right]^2 \rightarrow \min. \quad (8)$$

With Eq. (8) we derive the Lehr damping  $D = 0.0118$  and the small deflection eigenfrequency at  $f_0 = \omega_0/(2\pi) = 113.3 \text{ Hz}$ . Using the simulated mirror inertia  $J$ , we can now calculate the linear spring coefficient  $k_0 = J(2\pi f_0)^2 = 1.97 \times 10^{-6} \text{ Nm/rad}$  as well as the damping coefficient  $b = 2JD\omega_0 = 5.21 \times 10^{-11} \text{ Nms}$ . The  $Q$ -factor becomes  $Q = 1/(2D) = 53$ . Finally, the nonlinear spring characteristic ( $k_2 \approx 1.64 \times 10^{-5} \text{ Nm/rad}^3$ ) is determined with a finite element simulation, resulting in the matched stiffness curve with  $f_0$  in Fig. 10.

The capacitance derivative is parametrized by using the nonlinear torque equilibrium, Eq. (9), for each electrode.

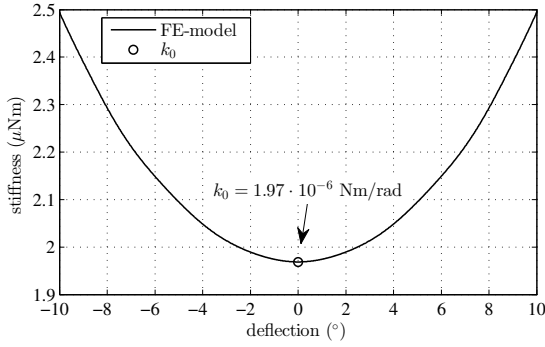


Figure 10: Nonlinear spring stiffness, Eq. (7)

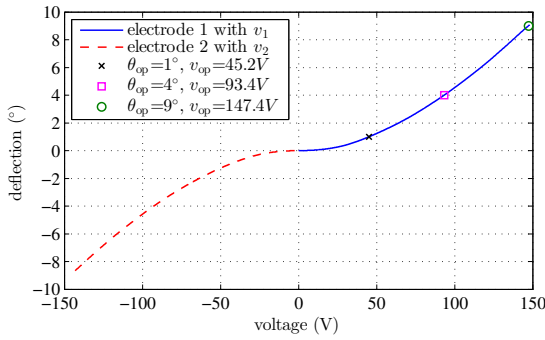


Figure 11: Measured static voltage-deflection characteristic  $v_n(\theta)$  applying a slow voltage sweep for both combs

Since the nonlinear spring moment has been determined, the capacitance derivatives (cf. Fig. 8b (measurement)) are given by Eq. (9) using the static voltage-deflection characteristic  $v_n(\theta)$  (cf. Fig. 11). The stray capacitance for the emerged comb angles is approximated by an exponential extrapolation as described in [40]. The straight line in Fig. 8b (measurement), demonstrates the resulting capacitance derivative with Eq. (9).

$$C'_1(\theta) = \frac{2\tau_s(\theta)}{v_1^2(\theta)} \quad \text{for } \theta \geq 0 \quad (9a)$$

$$C'_2(\theta) = \frac{2\tau_s(\theta)}{v_2^2(\theta)} \quad \text{for } \theta \leq 0 \quad (9b)$$

For the following control design we neglect the external torque  $\tau_{\text{ext}}$  in Eq. (6) because no known external disturbance, e.g. caused by the inner resonant axis, was observed yet.

### 3.3. System linearization

The nonlinear system Eq. (6) can be linearized at the operating point  $[\theta_{\text{op}}, v_{\text{op}}]$  and apply the Laplace transformation to receive the linear transfer function Eq. (10) for

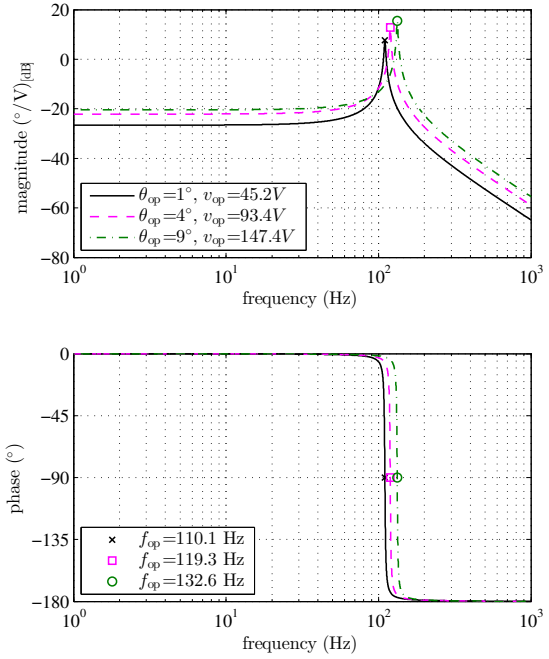


Figure 12: Bode diagram for linearized transfer function Eq. (10) at three operation points, cf. Fig. 11

the damped harmonic oscillator with the input voltage  $V(s)$  and the deflection output  $\Theta(s)$  according to [38, 65, 72].

$$G_{\text{op}}(s) = \frac{\Theta(s)}{V(s)} = \frac{K_{\text{el}}}{k(\theta_{\text{op}}) - k_{\text{el}}} \frac{1}{1 + 2d_{\text{op}} \frac{s}{\Omega_{\text{op}}} + \frac{s^2}{\Omega_{\text{op}}^2}}, \quad (10a)$$

$$K_{\text{el}} = C'(\theta_{\text{op}})v_{\text{op}}, \quad k_{\text{el}} = \frac{1}{2}C''(\theta_{\text{op}})v_{\text{op}}^2, \quad (10b)$$

$$d_{\text{op}} = \frac{1}{2} \frac{b}{k(\theta_{\text{op}}) - k_{\text{el}}} \Omega_{\text{op}}, \quad \Omega_{\text{op}}^2 = \frac{k(\theta_{\text{op}}) - k_{\text{el}}}{J} \quad (10c)$$

From the bode diagram in Fig. 12, we obtain the system's range in resonant frequency from about 110.1 Hz to 132.6 Hz.

### 3.4. Simulation

We validate the physical model Eq. (6) comparing the simulation with MATLAB/SIMULINK<sup>®</sup> with the measurement result for a step response as shown in Fig. 13. Simulation results with control on trajectories are presented in Fig. 26.

## 4. Trajectory design

The following section describes the design of optimized trajectories for quasi-static scanning. The scan application

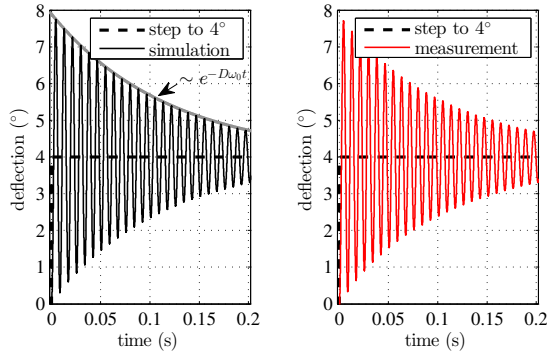


Figure 13: Step response to 4° with  $v_1 = 93.4$  V: simulation (left) and measurement (right), the maximum difference is 140 m°

requires near-triangular movement with constant speed, as shown in Fig. 4. To avoid residual oscillations of the high dynamic and low damped second order mass-spring system, we develop a jerk limitation for the command trajectory. In [40] we have shown, that the open-loop performance increases with lower specified maximum jerk. The trajectory is limited to the available torque given by the comb drive actuators to cope with the restriction of the unidirectional actuation. Furthermore this method prevents undesired overshoot and improves the closed-loop performance.

#### 4.1. Jerk limitation

A common polynomial trajectory design for flat systems [46, 73] is using fifth order polynomial splines for the reversal points, tested in [35]. Although this method satisfies the differential continuity until the second time derivative of the deflection angle, we observe high residual oscillation of the low-damped mirror system, because the jerk  $\ddot{\theta}(t) := j(t)$  is not limited. Therefore we implement a new design with third order polynomials given with Eq. (11) for  $n_{\text{seg}}$  segments, where the maximum jerk  $|\ddot{\theta}(t)| = j_{\text{max}}$  is constant.

$$\theta_{i+1}(t) = \bar{\theta}_i + \dot{\bar{\theta}}_i \cdot (t - t_i) + \frac{\ddot{\bar{\theta}}_i}{2} \cdot (t - t_i)^2 + \frac{\ddot{\bar{\theta}}_i}{6} \cdot (t - t_i)^3 \quad \text{for } t_i < t < t_{i+1} \quad \text{with } i = 0 \dots n_{\text{seg}} - 1 \quad (11)$$

For a given time period  $T$ , a maximum deflection  $\theta_{\text{max}}$  and a linear deflection  $\theta_{\text{lin}}$  the triangle trajectory is defined by Eq. (11) and the polynomial coefficients  $(\bar{\theta}_i, \dot{\bar{\theta}}_i, \ddot{\bar{\theta}}_i, \ddot{\bar{\theta}}_i)$  in Tab. 2 for each segment. Figure 14 illustrates the jerk-limited triangle trajectory, showing the *linear area* with constant velocity and the *upper/lower reversal* with third order polynomials and constant jerk. Table 2 is determined with Eq. (11) for the triangle shaped jerk-limited trajectory beginning at zero deflection (Fig. 14) and assuming the constants  $k_{\text{lin}} = \theta_{\text{lin}}/\theta_{\text{max}}$ ,  $\lambda_1 = 3 - k_{\text{lin}}$ ,  $\lambda_2 = 1 - k_{\text{lin}}$ .

Table 2: Polynomial coefficients for jerk-limited triangle shaped trajectory Eq. (11) with  $k_{\text{lin}} = \theta_{\text{lin}}/\theta_{\text{max}}$ ,  $\lambda_1 = 3 - k_{\text{lin}}$ ,  $\lambda_2 = 1 - k_{\text{lin}}$

$i$	$t_i/T$	$\bar{\theta}_i/\theta_{\text{max}}$	$\dot{\bar{\theta}}_i/\theta_{\text{max}}\lambda_1$	$\ddot{\bar{\theta}}_i/\theta_{\text{max}}\lambda_1^2$	$\ddot{\bar{\theta}}_i/\theta_{\text{max}}\lambda_1^3$
0	0	0	2	0	0
1	$\frac{k_{\text{lin}}}{2\lambda_1}$	$k_{\text{lin}}$	2	0	$-\frac{32}{27}$
2	$\frac{1}{4}$	1	0	$-\frac{8}{3}$	$\frac{32}{27}$
3	$\frac{1}{2} - \frac{k_{\text{lin}}}{2\lambda_1}$	$k_{\text{lin}}$	-2	0	0
4	$\frac{1}{2} + \frac{k_{\text{lin}}}{2\lambda_1}$	$-k_{\text{lin}}$	-2	0	$\frac{32}{27}$
5	$\frac{3}{4}$	-1	0	$\frac{8}{3}$	$-\frac{32}{27}$
6	$1 - \frac{k_{\text{lin}}}{2\lambda_1}$	$-k_{\text{lin}}$	2	0	0
7	1	0	2	0	0

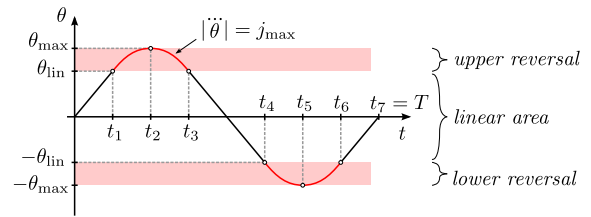


Figure 14: Jerk-limited triangle trajectory, cf. Eq. (11) and Tab. 2

#### 4.2. Limitations for unidirectional actuation

To ensure controllability, the desired trajectory must be designed in the limits of the mirror's controllable torque. Figure 15 shows the controllable electrostatic torques  $\tau_1(\theta, v_1)$  and  $\tau_2(\theta, v_2)$  from zero to maximum voltage using Eq. (6), while the maximum  $\tau_n(\theta, v_{\text{max}})$  is shown in bold lines. The spring torque  $\tau_s$  (cf. Eq. (7)) defining the maximum deflection acts against the electrostatic torques, thus the negative sign is used in Eq. (12) and Fig. 16. Note the mirror parameters identified in section 3.2. Due to the attractive electrostatic forces and the exponential decrease for emerged comb fingers, the effective controllable drive torque is approximately restricted to one direction for each

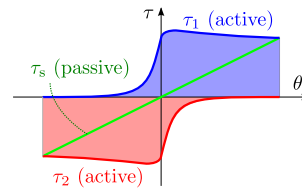


Figure 15: Active electrostatic drive torque  $\tau_1$  (blue),  $\tau_2$  (red) and passive spring torque  $\tau_s(\theta)$  (green) illustrating controllable areas

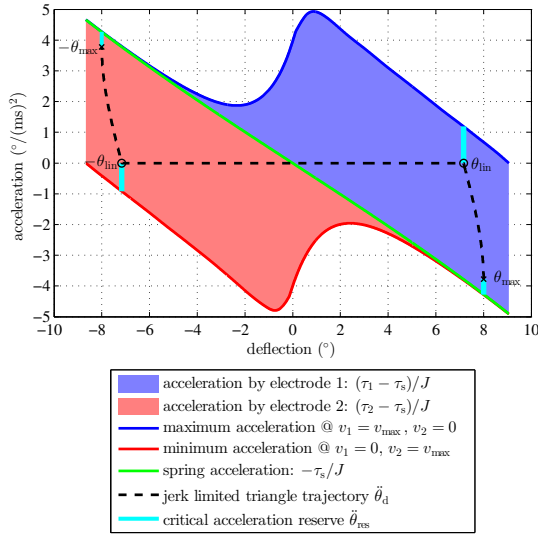


Figure 16: Controllable acceleration  $\ddot{\theta}(\theta, v_1, v_2)$  according Eq. (12) illustrating jerk limited trajectory  $\ddot{\theta}_d$  and critical reserve  $\ddot{\theta}_{res}$

comb, called *unidirectional* actuation.

We exploit an extended trajectory design considering the controllable acceleration, by matching the trajectory dynamics with the mirror's accessible acceleration. Eq. (12) denotes the mirror's acceleration as a function of the mirror angle  $\theta$  and the applied drive voltages  $v_1$  and  $v_2$ . For simplicity, we neglect the very small damping torque  $\tau_D$ .

$$\ddot{\theta}(\theta, v_1, v_2) = \frac{1}{J} \left( \tau_1(\theta, v_1) + \tau_2(\theta, v_2) - \tau_s(\theta) \right) \quad (12)$$

Figure 16 illustrates the controllable acceleration Eq. (12) of electrode 1 and electrode 2; therein we have to design the trajectory and its acceleration  $\ddot{\theta}_d$  respectively.

By defining a torque *reserve*  $\tau_{res} := J\ddot{\theta}_{res}$ , we intent to allow the feedback controller  $\Lambda$  a minimum torque or acceleration with  $\ddot{\theta}_{res} \equiv \max(\Lambda)$  to correct disturbances. The dashed line in Fig. 16 represents the desired trajectory considering this control reserve in acceleration. With help of Fig. 16, we derive the following two criteria for the jerk limited trajectory:

- 1) at maximum deflection  $\theta_{max}$ :

$$\ddot{\theta}_{max}^r := \frac{\tau_s(\theta_{max}) - \tau_{res}}{J}, \quad (13)$$

- 2) at linear deflection  $\theta_{lin}$ :

$$k_{lin}^r := \min(k_{lin,1}^r, k_{lin,2}^r) \quad \text{with} \quad (14a)$$

$$k_{lin,n}^r := 1 - \frac{2\tau_{res}}{|C'_n(\theta_{max})|v_{max}^2}, \quad n = 1, 2. \quad (14b)$$

8

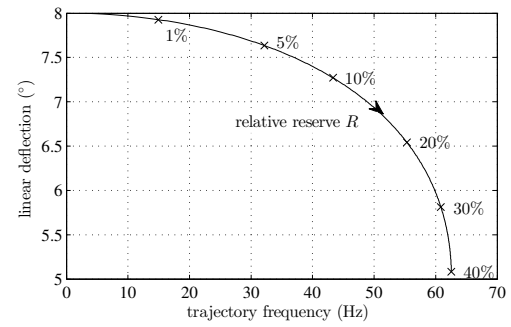


Figure 17: Resulting relative reserve  $R$  between linear deflection  $\theta_{lin}$  and trajectory frequency  $f = 1/T$  with  $\theta_{max} = 8^\circ$

Eq. (13) describes the maximum trajectory acceleration at  $\theta_{max}$  towards the spring torque including the torque reserve. Eq. (14) restricts the linear area  $k_{lin} = \theta_{lin}/\theta_{max}$  considering the trajectory acceleration at  $\theta_{lin}$  towards the electrostatic acceleration with maximum drive voltage  $v_{max}$ . Due to small differences between the comb capacitances the minimum  $k_{lin}^r$  for both comb electrodes is chosen, supposing similar capacitance derivatives at  $\theta_{max}$  and  $\theta_{lin}$  with  $C'_1(\theta_{max}) \approx C'_1(\theta_{lin})$  and  $|C'_2(-\theta_{max})| \approx |C'_2(-\theta_{lin})|$ .

Finally, we describe the jerk-limited trajectory being restricted with the torque reserve  $\tau_{res}$  towards the limits of the controllability with Eq. (11) and polynomial coefficients in Tab. 2 by replacing  $(T, \lambda_1, \lambda_2)$  with  $(T^r, \lambda_1^r, \lambda_2^r)$  from Eq. (15).

$$T^r = \sqrt{\frac{8 \frac{\theta_{max}}{\ddot{\theta}_{max}^r} \lambda_1^{r2}}{3 \frac{\theta_{max}}{\ddot{\theta}_{max}^r} \lambda_2^r}}, \quad \lambda_1^r = 3 - k_{lin}^r, \quad \lambda_2^r = 1 - k_{lin}^r \quad (15)$$

Figure 17 demonstrates the extended trajectory design for an exemplary triangle trajectory with  $\theta_{max} = 8^\circ$  using the relative reserve  $R$ :

$$R := \frac{\tau_{res}}{\tau_s(\theta_{max})}. \quad (16)$$

## 5. Flatness-based control design

In this section we apply the straight forward *flatness-based* control design method for the nonlinear quasi-static micro mirror system using the state space representation as introduced in [41, 42] and adapt a global extended Luenberger observer.

### 5.1. State space model and flatness

First we define the nonlinear dual-input-single-output (DISO) system for the state  $\mathbf{x} = (x_1, x_2) = (\theta, \dot{\theta})$ :

$$\dot{\mathbf{x}}(t) = \mathbf{f}(\mathbf{x}, v_1, v_2). \quad (17)$$



and denote the state space model for the differential Eq. (6) as follows:

$$\dot{x}_1 = x_2 \quad (18a)$$

$$\dot{x}_2 = -\frac{b}{J}x_2 - \frac{\tau_s(x_1)}{J} + \underbrace{\frac{C'_1(x_1)}{2J}v_1^2 + \frac{C'_2(x_1)}{2J}v_2^2}_{:=u} \quad (18b)$$

Let us then assemble the voltage input of both combs in a new input  $u$  with Eq. (19).

$$u := \frac{1}{2J}C'_1(x_1)v_1^2 + \frac{1}{2J}C'_2(x_1)v_2^2 \quad (19)$$

As customary in position control, we define the mirror deflection angle as our system output  $y = x_1 = \theta$  and with Eq. (19) we get the single-input-single-output (SISO) system Eq. (20).

$$\dot{x}_1 = x_2 \quad (20a)$$

$$\dot{x}_2 = -\frac{b}{J}x_2 - \frac{\tau_s(x_1)}{J} + u \quad (20b)$$

$$y = x_1 \quad (20c)$$

The system Eq. (20) is *differentially flat* as shown in [35], because the state vector  $\mathbf{x}$  and the input  $u$  can be written as a function of the differentially independent variable  $y$ , also called *flat output*, and its derivatives, cf. Eq. (21).

$$u(y, \dot{y}, \ddot{y}) = \ddot{y} + \frac{b}{J}\dot{y} + \frac{\tau_s(y)}{J}. \quad (21)$$

According to [74] the flat system representation also results directly from the Lagrange Eq. (3) for the general coordinate  $\theta$ , the system input Eq. (19) and the flat output  $y = \theta$ .

### 5.2. Open-loop control

For the flatness-based open-loop control we determine the desired input  $u_d$  with Eq. (22) for a given reference trajectory  $(\theta_d, \dot{\theta}_d, \ddot{\theta}_d)$  analog to Eq. (21):

$$u_d = \ddot{\theta}_d + \frac{b}{J}\dot{\theta}_d + \frac{\tau_s(\theta_d)}{J}. \quad (22)$$

*Comb switch.* To calculate the command voltages  $(v_1, v_2)$ , we have to switch between the comb drives according to the desired direction of the input  $u_d$ . Due to the unidirectional actuation (cf. section 4.2) we activate comb 1 with  $v_1$  for positive acceleration and comb 2 with  $v_2$  for positive acceleration. With Eq. (19) we get the *comb switch* relation Eq. (23):

$$v_1(u_d, \theta_d) = \begin{cases} \sqrt{\frac{2Ju_d}{C'_1(\theta_d)}} & \text{for } u_d > 0 \\ 0 & \text{for } u_d \leq 0 \end{cases} \quad (23a)$$

$$v_2(u_d, \theta_d) = \begin{cases} 0 & \text{for } u_d > 0 \\ \sqrt{\frac{2Ju_d}{C'_2(\theta_d)}} & \text{for } u_d \leq 0 \end{cases} \quad (23b)$$

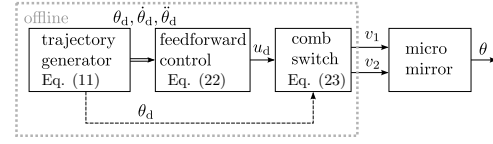


Figure 18: Schematic of open-loop control

Figure 18 illustrates the open-loop structure given by the trajectory generator with Eq. (11), the flatness-based input Eq. (22) and the comb switch Eq. (23) calculating the voltage output. These command voltages for the open-loop triangle trajectory are shown in Fig. 23.

### 5.3. Closed-loop control

The accuracy of the open-loop control is limited by an imprecise model structure and model parameter as well as external dynamic effects, like temperature changes, that lead to undesired oscillation on the desired trajectory [35, 38]. To compensate these residual oscillations of the mirror, we close the control loop by measuring in real-time the actual mirror deflection  $\theta$  and adapting the system input  $u$  according to the determined position error  $e(t) = \theta_d(t) - \theta(t)$ . Any controller  $\Lambda$ , that stabilizes asymptotically the error can be added to the system open-loop input  $u_d$ . Thus, we introduce the controlled input  $u \equiv u^*$ :

$$u^* = u_d + \Lambda(e, \dot{e}). \quad (24)$$

We apply the *extended PID<sup>k</sup> control* Eq. (25) proposed in [75–77] to stabilize the system around the desired trajectory with the control gains  $[K_P, K_I, K_D] > 0$ .

$$\Lambda(e(t), \dot{e}(t)) = K_P e(t) + K_I \int_0^t e(\tau) d\tau + K_D \dot{e}(t) \quad (25)$$

Stability for the system Eq. (20) in closed-loop with control input Eq. (24) can be proven for bounded initial errors towards the desired trajectory [75]. Considering the error vector  $\mathbf{e} = [e_0, e_1, e_2] = [\int_0^t e(\tau) d\tau, e, \dot{e}]$ , we linearize the system around the desired trajectory ( $\mathbf{e} = 0$ ), that leads to the linearized error matrix  $\mathbf{e}_\delta$  in Eq. (26).

$$\dot{\mathbf{e}}_\delta = \underbrace{\begin{pmatrix} 0 & 1 & 0 \\ 0 & 0 & 1 \\ -K_I & -K_P - \frac{k_0}{J} - \frac{k_2}{J}\theta_d^2 & -K_D - \frac{b}{J} \end{pmatrix}}_{\mathbf{E}} \mathbf{e}_\delta. \quad (26)$$

The closed-loop control system is stable, when all eigenvalues of  $\mathbf{E}$  in Eq. (26) are negative. This is fulfilled, when choosing positive control gains and  $K_I < K_P K_D$ , since the Hurwitz matrices of the characteristic polynomial

$\det(s\mathbf{I} - \mathbf{E})$  with the identity matrix  $\mathbf{I}$  are

$$H_1 = K_D + \frac{b}{J} \quad (27a)$$

$$H_2 = \left(K_D + \frac{b}{J}\right) \left(K_P + \frac{k_0}{J} + \frac{k_2}{J}\theta_d^2\right) - K_I \quad (27b)$$

$$H_3 = K_I H_2. \quad (27c)$$

Nevertheless sensor noise and mechanical finger stability limits the maximum applicable control gains.

The control gains effectuate different system behaviors and were adjusted manually for the triangle trajectory in the following order:

1. The derivative correction term  $K_D \dot{e}(t)$  with the error  $\dot{e} = \dot{\theta}_d - \dot{\hat{\theta}}$  mainly reduces oscillations, but introduces a time shift, that leads to a constant error offset.
2. The proportional correction term  $K_P e(t)$  decreases the absolute error and reinforces oscillations.
3. The integral correction term  $K_I \int_0^t e(\tau) d\tau$  diminishes the deflection offset relating to the integral of an entire period, comparable to the elimination of the stationary error at steady state.

Since the derivation of the inherent noisy measurement feedback aggravates the noise, we implement a global extended Luenberger observer (section 5.4) to estimate the mirror state. In analogy to open-loop Eq. (23), we employ the comb switch Eq. (28) for the stabilized input  $u^*$  using the observed deflection  $\hat{\theta}$ .

$$v_1(u^*, \hat{\theta}) = \begin{cases} \sqrt{\frac{2Ju^*}{C_1'(\hat{\theta})}} & \text{for } u^* > 0 \\ 0 & \text{for } u^* \leq 0 \end{cases} \quad (28a)$$

$$v_2(u^*, \hat{\theta}) = \begin{cases} 0 & \text{for } u^* > 0 \\ \sqrt{\frac{2Ju^*}{C_2'(\hat{\theta})}} & \text{for } u^* \leq 0 \end{cases} \quad (28b)$$

Figure 19 outlines the schematic of the implemented flatness-based closed-loop control. While the blocks *extended PID control*, *comb switch* and *observer* have to be processed in real-time, the *trajectory generator* and *feed forward control* can be calculated beforehand offline.

#### 5.4. Global extended Luenberger observer

For estimating the mirror angular velocity  $\dot{\theta}$ , we design a global extended Luenberger observer [74, 78–80], shown in Fig. 20. The observer can be interpreted as a virtual copy of the real system, that gets an equivalent input and corrects its state  $\hat{x}$  with the error  $\hat{e} = \hat{\theta} - \theta$  towards the real system.

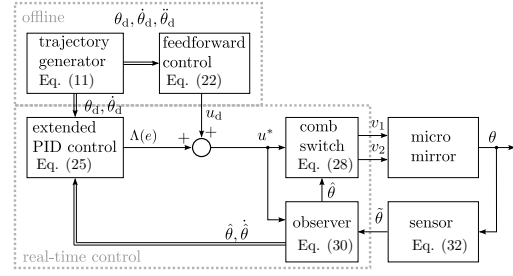


Figure 19: Schematic of flatness-based closed-loop control

First, let us write Eq. (20) in matrix notation:

$$\dot{x} = \underbrace{\begin{pmatrix} 0 & 1 \\ 0 & -\frac{b}{J} \end{pmatrix}}_{\mathbf{A}} x + \underbrace{\begin{pmatrix} 0 \\ 1 \end{pmatrix}}_{\mathbf{B}} \alpha(x_1, u) \quad (29a)$$

$$y = \underbrace{\begin{pmatrix} 1 & 0 \end{pmatrix}}_{\mathbf{C}^T} x \quad (29b)$$

$$\text{with } \alpha(x_1, u) = -\frac{\tau_s(x_1)}{J} + u. \quad (29c)$$

In Eq. (29) all nonlinearities are concentrated in  $\alpha(x_1, u)$  to get the system representation, known for linear systems with the system matrix  $\mathbf{A}$ , the input matrix  $\mathbf{B}$  and the output matrix  $\mathbf{C}^T$ , cf. Fig. 20.

We obtain the global extended Luenberger observer by reinterpreting the system representation Eq. (29) with the observer state  $x \rightarrow \hat{x}$ , the observer output  $y \rightarrow \hat{y}$  and finally adding a stabilizing observer gain  $\mathbf{L} = (l_1, l_2)^T$  to correct the observer error  $\hat{e} = \hat{y} - y$ .

$$\dot{\hat{x}} = \underbrace{\begin{pmatrix} 0 & 1 \\ 0 & -\frac{b}{J} \end{pmatrix}}_{\mathbf{A}} \hat{x} + \underbrace{\begin{pmatrix} 0 \\ 1 \end{pmatrix}}_{\mathbf{B}} \alpha(x_1, u) + \mathbf{L} \hat{e} \quad (30a)$$

$$\hat{y} = \underbrace{\begin{pmatrix} 1 & 0 \end{pmatrix}}_{\mathbf{C}^T} \hat{x} \quad (30b)$$

$$\text{with } \alpha(x_1, u) = -\frac{\tau_s(x_1)}{J} + u \quad (30c)$$

Figure 20 illustrates the system representation Eq. (29) and the designed observer Eq. (30). For the observer error we get the differential equation:

$$\dot{\hat{e}} = (\mathbf{A} - \mathbf{L}\mathbf{C}^T) \hat{e}. \quad (31)$$

To find an asymptotic stable rest position with  $\hat{e} = 0$ , we place the poles of Eq. (31) with the Ackermann formula [81] at  $p_{1,2} = 20\omega_0 = 1423 \text{ s}^{-1}$  resulting in  $\mathbf{L} = (-28443 \text{ s}^{-1}, -202055421 \text{ s}^{-2})^T$ .

## 6. Model validation and experimental results

In the following section we evaluate the proposed flatness-based control methods for the quasi-static axis

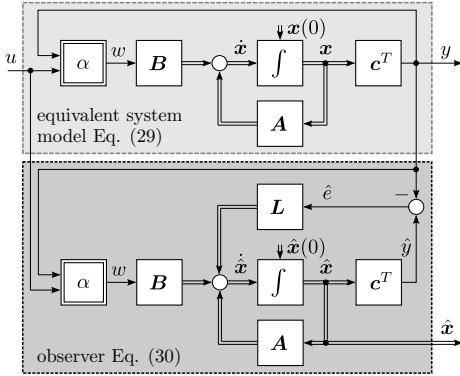


Figure 20: Schematic of system model with global extended Luenberger observer

of the 2D quasi-static/resonant microscanner, presented in section 2, with an experimental setup using a real-time system and optical feedback to measure the instantaneous mirror deflection. All following experiments have been realized with a jerk-limited triangle trajectory with  $\theta_{\max} = 5^\circ$  maximum and  $\theta_{\min} = 4^\circ$  linear deflection, cf. section 4.

#### 6.1. Experimental setup

Figure 21 illustrates the realized experimental setup.

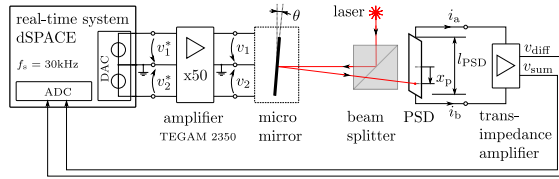


Figure 21: Experimental setup

The experimental setup consists of a real-time controller (DS1007) from dSPACE®, that provides a digital-analog-converter (DS2004) for the control output voltages and an analog-digital-converter (DS2102) for the measurement feedback. The control loop is processed with a sampling frequency of  $f_s = 30 \text{ kHz}$ . The  $50\times$  voltage amplifier TEGAM® 2350 generates the required comb drive voltages  $v_1$  and  $v_2$  up to  $150 \text{ V}$ , thus we consider the gain  $v^*/v = 0.02$  for the output voltage.

The position feedback is realized with a laser, that is deflected by the micro mirror on the *position sensitive device* (PSD) DL400-7PCBA from SILICON SENSORS® through a beam splitter. The laser spot, detected on the PSD, results in two photo currents  $i_a$  and  $i_b$ , that are converted with a transimpedance amplifier to the difference voltage  $v_{\text{diff}} \sim i_a - i_b$  and the sum voltage  $v_{\text{sum}} \sim i_a + i_b$ , limited at  $85 \text{ kHz}$  bandwidth. The mirror deflection angle  $\theta$  is evaluated with Eq. (32), where  $l_{\text{PSD}}$  denotes the length of the PSD and  $d_{\text{PSD}}$  is the distance between the mirror and

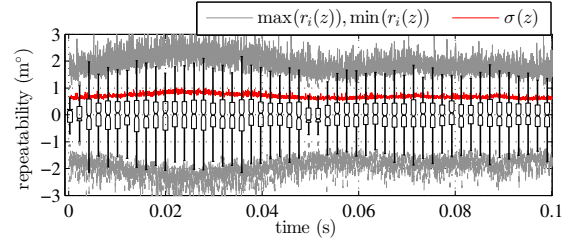


Figure 22: Repeatability limits  $\max(r_i(z))$ ,  $\min(r_i(z))$ , standard deviation  $\sigma(z)$  and boxplot for a 10 Hz triangle trajectory

the PSD, including a correction for the beam refraction in the beam splitter. The nonlinearity of the PSD is corrected with a reference calibration.

$$\tilde{\theta} = \frac{1}{2} \arctan \left( \frac{l_{\text{PSD}} v_{\text{diff}}}{2d_{\text{PSD}} v_{\text{sum}}} \right) \quad (32)$$

#### 6.2. Performance metrics

To compare the performance of the experimental results, we define the two metrics *mean error* Eq. (33a) and *repeatability* Eq. (33b) for 200 periods with the sampling variable  $z$  and  $n = f_s \cdot T$  samples for the trajectory time period  $T$ .

$$\text{mean error: } e(z) = \frac{1}{200} \sum_{i=1}^{200} (\tilde{\theta}_i(z) - \theta_d(z)) \quad (33a)$$

$$\text{repeatability: } r_i(z) = \tilde{\theta}_i(z) - \frac{1}{200} \sum_{i=1}^{200} \tilde{\theta}_i(z) \quad (33b)$$

with  $z = 0, 1, \dots, n$

The repeatability of about  $\pm 3 \text{ m}^\circ$  peak-to-peak shown in Fig. 22 is equivalent for all measurements and mainly represents a high frequency noise of the PSD with

$$\sigma(z) = \sqrt{\sum_{i=0}^{200} r_i^2(z)}, \quad \sigma_{\max} = \max(\sigma(z)). \quad (34)$$

#### 6.3. Open-loop control results

An obvious advantage of the open-loop control is, that no sensor feedback is required and all calculations can be processed offline. We achieve considerable good results by driving the mirror with feed forward control as shown in Fig. 23. Compared to linear prefilter [38] or input shaping [39], the proposed flatness-based open-loop control (section 5.2) improves the results (cf. Fig. 24) since it incorporates the nonlinearities of the spring stiffness and the drive capacitance, that are calibrated by static measurements. Nevertheless, the result in Fig. 23 shows a substantial residual oscillation with the mirror's eigenfrequency of  $\pm 300 \text{ m}^\circ$

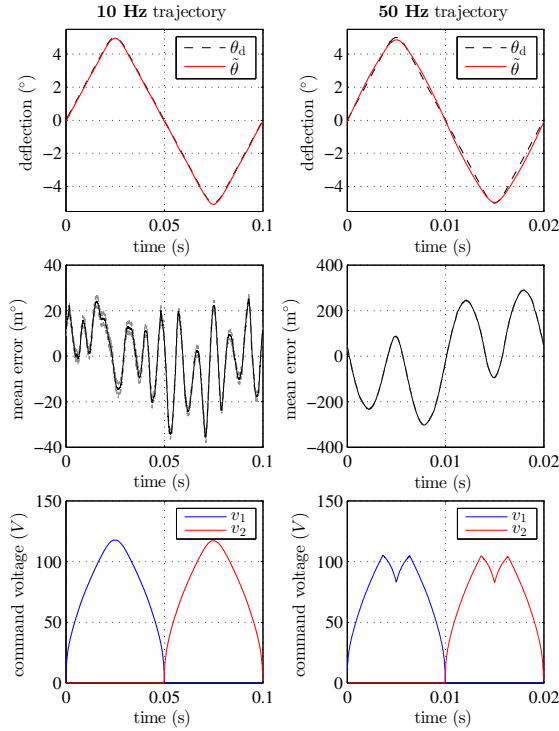


Figure 23: Experimental result for flatness-based **open-loop** control, showing the mean error and the command voltages according to Eq. (22) and (23). The two shadowed lines besides the main signal describe the min. and max. signal of all 200 periods measured.

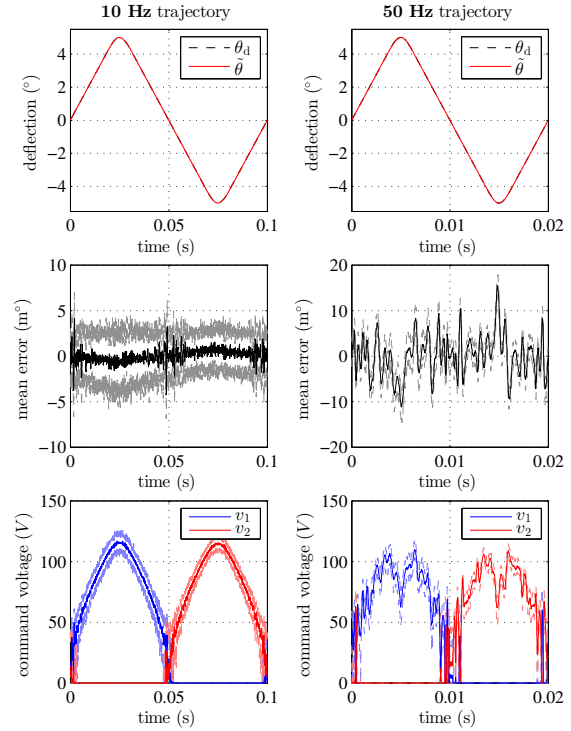


Figure 25: Experimental result for flatness-based **closed-loop** control, showing the mean error and the command voltages according to Eq. (22), (24), (28). The two shadowed lines besides the main signal describe the min. and max. signal of all 200 periods measured.

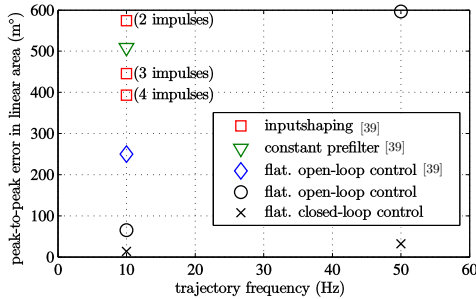


Figure 24: Comparison of errors for different control strategies: results from Tab. 3 and input shaping, constant prefilter, flatness-based control from [39]

for the 50 Hz trajectory, that is ten times higher than for the 10 Hz with  $\pm 30 \text{ m}^\circ$ . That depicts the limit for the open-loop control strategy, because model inaccuracies and external disturbances cannot be compensated.

#### 6.4. Closed-loop control results

The flatness-based closed-loop control significantly reduces the control error, as shown in Fig. 25 with about  $\pm 7 \text{ m}^\circ$  for a 10 Hz trajectory and about  $\pm 16 \text{ m}^\circ$  for a 50 Hz trajectory, as summarized in Tab. 3. Here the control gains  $[K_P, K_I, K_D]$  at  $[10^8 \text{ s}^{-2}, 10^{11} \text{ s}^{-3}, 10^4 \text{ s}^{-1}]$  have been applied. Due to closing the loop, the residual oscillations at the mirror's eigenfrequency around 113.3 Hz are eliminated, which is a major achievement regarding the trajectory tracking with quasi-static micro mirrors.

Comparing closed-loop results with open-loop results, we figure out an increase of the signal noise, which is fed into the control loop by the position measurement with PSD. The signal noise is illustrated by shadowed lines in Fig. 23 and Fig. 25 beside the main signal. Since the mirror does weakly respond on high frequent input signals (cf. Fig. 12) the trajectory precision is not effected. Supplementary low-pass filters could reduce the measurement noise of  $\theta$ , but they also introduce additional time delays influencing the tracking precision.

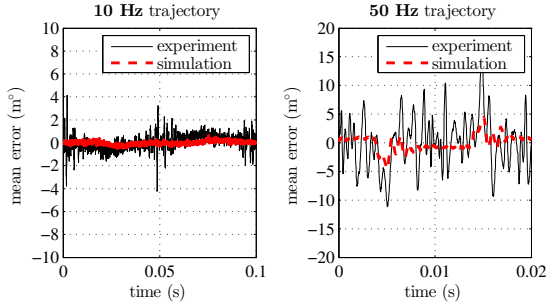


Figure 26: Comparison of **simulation vs. experimental** errors

*Verification of simulation results.* We determine a high agreement of the simulation results from the MATLAB/SIMULINK® model with the experimental results, which verifies the presented physical modeling, as displayed in Fig. 26 for a triangle trajectory with 10 Hz and 50 Hz. The PSD measurement noise in the simulation is represented by

$$\theta_{\text{noise}}(s) = \frac{4\sigma_{\text{max}}^2 d_b T_b}{1 + 2d_b T_b s + T_b^2 s^2}, \quad T_b = \frac{1}{2\pi f_b} \quad (35)$$

adding the colored noise  $\sigma_{\text{max}} = 1 \text{ m}^\circ$ , derived from Fig. 22 with Eq. (34) and  $d_b = 0.7$ ,  $f_b = 15 \text{ kHz}$  for a 2<sup>nd</sup> order bandwidth filter as described in [65].

## 7. Performance evaluation

Comparing the error of closed-loop and open-loop control, cf. Tab. 3, we state a significant improvement of the mirror's trajectory tracking accuracy of factor 4 for the 10 Hz trajectory and of factor 18 for the 50 Hz trajectory for closed-loop control. While the open-loop control is limited to the precision of the mirror model and its parameter, the closed-loop control compensates model inaccuracies as well as external disturbances or other influences like temperature drift in the mirror device when using the PSD feedback.

Table 3: Experimental results for open-loop vs. closed-loop control from Fig. 25 and Fig. 23 comprising the peak-to-peak (ptp) error

	open-loop	closed-loop
ptp error @ 10 Hz	65.2 m°	13.9 m°
ptp error @ 50 Hz	596.6 m°	31.7 m°

In addition, we determine exceeding errors with open-loop control for trajectory frequencies  $f$ , whose higher harmonics correspond to the fundamental mirror eigenfrequency  $f_0^*$  with the relation  $f \approx \frac{1}{m} f_0^*$  for  $m = 1, 2, \dots$ ,

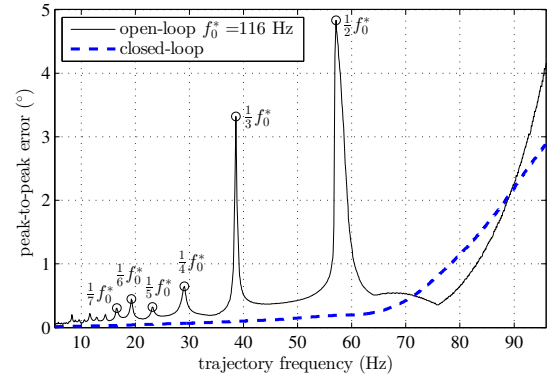


Figure 27: Peak-to-peak trajectory error from experimental data varying the trajectory frequency  $f$  in open-loop and closed-loop control, showing the interference of higher trajectory harmonics in open-loop

as shown in Fig. 27. We attribute this effect to the interference of these higher harmonics  $m \cdot f$  of the applied triangle trajectory with the mirror's eigenfrequency near  $f_0^* = 116 \text{ Hz}$ , that constitutes a mean frequency passed through while following the trajectory, considering the non-linearity of the eigenfrequency, cf. Eq. (10c). Therefore, we suggest choosing a basic trajectory frequency in between the subharmonics of the mirror's eigenfrequency when applying open-loop control. The closed-loop control achieves to suppress this effect.

## 8. Conclusion

Quasi-static microscanner with electrostatic staggered comb drive (SVC) are particularly advantageous for high precision laser tracking and raster scanning tasks, but must be controlled to eliminate the eigenfrequency oscillation of the very low damped spring-mass-system. We have demonstrated the application of a jerk-limited trajectory design within the actuator limitation and verified a flatness-based open-loop and closed-loop control, that achieves a total precision better than  $14 \text{ m}^\circ$  for a triangle scan with 10 Hz and  $10^\circ$  mechanical scan angle. This means we can resolve at least  $10^\circ / 14 \text{ m}^\circ = 714$  distinguishable deflections (or pixels) for the quasi-static axis in a raster scan.

*Outlook.* The presented micro mirror has an intrinsic position sensor, based on the piezo-resistive effect, that is currently tested as position feedback for feedback control [57, 58]. Typical scanning application often require repeated trajectories; therefore *repetitive controller* (RC) [82] or *iterative learning controller* (ILC) [83, 84] are expected as promising candidates for improving the results for feedback control.



## Acknowledgments

We would like to thank Veit Hagenmeyer (Karlsruhe Institute of Technology, Head of Institute for Applied Computer Science, Germany) for his support with the stability analysis and Kenta Seki (Nagoya Institute of Technology, Japan) for critical discussions on this paper.

## References

- [1] H. Cho, *Optomechatronics: Fusion of Optical and Mechatronic Engineering*, Mechanical and Aerospace Engineering Series, CRC press, 2005.
- [2] M. Motamedi, *MOEMS: Micro-opto-electro-mechanical Systems*, Vol. PM126 of Press Monographs, SPIE Press Book, 2005.
- [3] T. Sandner, T. Grasshoff, M. Wildenhain, H. Schenk, Synchronized microscanner array for large aperture receiver optics of LIDAR systems, in: W. P. Harald Schenk (Ed.), *Proc. of SPIE, MOEMS and Miniaturized Systems IX*, Vol. 7594, 2010, pp. 75940C–75940C–12.
- [4] H. Gröger, J. Knobbe, T. Egloff, M. Althaus, M. Scholles, H. Schenk, Scanning photon microscope based on a MEMS 2D scanner mirror, in: D. L. Dickensheets, H. Schenk, W. Piyawatnametha (Eds.), *Proc. of SPIE, MOEMS and Miniaturized Systems VIII*, Vol. 7208, 2009, pp. 72080O–72080O–11.
- [5] U. Schelinski, J. Knobbe, H.-G. Dallmann, H. Gröger, M. Förster, M. Scholles, M. Schwarzenberg, R. Rieske, MEMS-based laser scanning microscope for endoscopic use, in: W. P. Harald Schenk (Ed.), *Proc. of SPIE, MOEMS and Miniaturized Systems X*, Vol. 7930, 2011, pp. 793004–793004–10.
- [6] J. Grahmann, A. Merten, R. Ostendorf, M. Fontenot, D. Bleh, H. Schenk, H.-J. Wagner, Tunable External Cavity Quantum Cascade Lasers (EC-QCL): an application field for MOEMS based scanning gratings, in: W. Piyawatnametha, Y.-H. Park (Eds.), *Proc. of SPIE, MOEMS and Miniaturized Systems XIII*, Vol. 8977, 2014, pp. 897708–897708–11.
- [7] A. C.-L. Hung, H. Y.-H. Lai, T.-W. Lin, S.-G. Fu, M. S.-C. Lu, An electrostatically driven 2d micro-scanning mirror with capacitive sensing for projection display, *Sensors and Actuators A: Physical* 222 (2015) 122 – 129.
- [8] D. Jung, T. Sandner, D. Kallweit, H. Schenk, Vertical comb drive microscanners for beam steering, linear scanning, and laser projection applications, in: W. N. Harald Schenk, Wibool Piyawatnametha (Ed.), *Proc. of SPIE, MOEMS and Miniaturized Systems XI*, Vol. 8252, 2012, pp. 82520U–82520U–10.
- [9] A. Wolter, H. Schenk, E. Gaumont, H. Lakner, MEMS microscanning mirror for barcode reading: from development to production, in: D. L. D. Hakan Urey (Ed.), *Proc. of SPIE, MOEMS Display and Imaging Systems II*, Vol. 5348, 2004, pp. 32–39.
- [10] M. Scholles, A. Brauer, K. Frommhagen, C. Gerwig, B. Hofer, E. Jung, H. Lakner, H. Schenk, B. Schneider, P. Schreiber, A. Wolter, Miniaturized optical module for projection of arbitrary images based on two-dimensional resonant micro scanning mirrors, in: S. F. Sagan, G. F. Marshall (Eds.), *Proc. of SPIE, Optical Scanning*, Vol. 5873, 2005, pp. 72–83.
- [11] H. Urey, Torsional mems scanner design for high-resolution scanning display systems, in: *Proc. SPIE 4773, Optical Scanning*, Vol. 4773, 2002, pp. 27–37.
- [12] R. B. Sprague, T. Montague, D. Brown, Bi-axial magnetic drive for scanned beam display mirrors, in: *Proc. SPIE 5721, MOEMS Display and Imaging Systems III*, Vol. 5721, 2005, pp. 1–13.
- [13] D. A. Sabo, D. Brunner, A. Engelmayer, Advantages of digital servo amplifiers for control of a galvanometer based optical scanning system, in: *Proc. of SPIE, Optical Scanning*, Vol. 5873, 2005, pp. 113–120.
- [14] Z. Hao, *Mems/Nems: Handbook Techniques and Applications*, Springer US, Boston, MA, 2006, Ch. Techniques in the Design of Micro-Machined Electrostatic Torsion Micro-Mirrors and Their Applications, pp. 1655–1717.
- [15] J. J. Gorman, B. Shapiro, *Feedback Control of MEMS to Atoms*, Vol. VIII, Springer, 2012.
- [16] S. Weinberger, T. T. Nguyen, C. Ament, M. Hoffmann, Quasi-static micromirror with enlarged deflection based on aluminum nitride thin film springs, *Sensors and Actuators A: Physical* 210 (2014) 165–174.
- [17] G. Zhu, L. Saydy, M. Hosseini, J. F. Chianetta, Y. A. Peter, A robustness approach for handling modeling errors in parallel-plate electrostatic mems control, *Journal of Microelectromechanical Systems* 17 (6) (2008) 1302–1314.
- [18] G. Zhu, J. Penet, L. Saydy, Robust control of an electrostatically actuated mems in the presence of parasitics and parametric uncertainties, in: *American Control Conference*, 2006, pp. 1233–1238.
- [19] Y. Bai, J. T. W. Yeow, P. Constantinou, S. Damaskinos, B. C. Wilson, A 2-d micromachined soi mems mirror with sidewall electrodes for biomedical imaging, *IEEE/ASME Transactions on Mechatronics* 15 (4) (2010) 501–510.
- [20] C. Bai, J. Huang, Multistep-shaping control based on the static and dynamic behavior of nonlinear optical torsional micromirror, *Optical Engineering* 53 (5) (2014) 057109.
- [21] R. A. Conant, J. T. Nee, K. Y. Lau, R. S. Muller, A flat high-frequency scanning micromirror, in: *Hilton Head Solid-State Sensor and Actuator Workshop 2000*, Transducer Research Foundation, 2000, pp. 6–9.
- [22] P. Patterson, D. Hah, H. Nguyen, H. Toshiyoshi, R. min Chao, M. Wu, A scanning micromirror with angular comb drive actuation, in: *The Fifteenth IEEE International Conference on Micro Electro Mechanical Systems*, 2002, pp. 544–547.
- [23] V. Milanovic, K. Castelino, Sub-100us settling time and low voltage operation for gimbal-less two-axis scanners, *IEEE LEOS Optical MEMS*, Takamatsu, Japan, 2004.
- [24] V. Milanovic, Improved control of the vertical axis scan for mems projection displays, in: *IEEE/LEOS International Conference on Optical MEMS and Nanophotonics*, 2007, pp. 89–90.
- [25] D. Hah, P. Patterson, H. Nguyen, H. Toshiyoshi, M. Wu, Theory and experiments of angular vertical comb-drive actuators for scanning micromirrors, *IEEE Journal of Selected Topics in Quantum Electronics* 10 (3) (2004) 505–513.
- [26] S. Kwon, V. Milanovic, L. P. Lee, Vertical combdrive based 2-D gimbaled micromirrors with large static rotation by backside island isolation, *IEEE Journal of Selected Topics in Quantum Electronics* 10 (3) (2004) 498–504.
- [27] H. Chen, M. Pallapa, W. J. Sun, Z. D. Sun, J. T. W. Yeow, Nonlinear control of an electromagnetic polymer mems hard-magnetic micromirror and its imaging application, *Journal of Micromechanics and Microengineering* 24 (4) (2014) 045004.
- [28] S. Pannu, C. Chang, R. S. Muller, A. P. Pisano, Closed-loop feedback-control system for improved tracking in magnetically actuated micromirrors, in: *International Conference on Optical MEMS*, IEEE/LEOS, 2000, pp. 107–108.
- [29] H. Zhang, D. Xu, X. Zhang, Q. Chen, H. Xie, S. Li, Model-based angular scan error correction of an electrothermally-actuated mems mirror, *Sensors* 15 (12) (2015) 29840.
- [30] L. Wu, H. Xie, A large vertical displacement electrothermal bimorph microactuator with very small lateral shift, *Sensors and Actuators A: Physical* 145 - 146 (2008) 371 – 379.
- [31] B. Bhikkaji, M. Ratnam, A. J. Fleming, S. O. R. Moheimani, High-performance control of piezoelectric tube scanners, *IEEE Transactions on Control Systems Technology* 15 (5) (2007) 853–866.
- [32] U. Baran, D. Brown, S. Holmstrom, D. Balma, W. O. Davis, P. Mural, H. Urey, Resonant pzt mems scanner for high-resolution displays, *Journal of Microelectromechanical Systems* 21 (6) (2012) 1303–1310.
- [33] A. Tortschanoff, A. Frank, M. Wildenhain, T. Sandner, A. Kenda, Optical position encoding and phase control of an electrostatically driven two-dimensional MOEMS scanner at two resonant modes, *Journal of Micro/Nanolithography, MEMS, and MOEMS* 10 (3) (2011) 033006–033006–9.
- [34] T. Sandner, D. Jung, D. Kallweit, T. Grasshoff, H. Schenk,

- Microscanner with vertical out of plane combdrive, in: International Conference on Optical MEMS and Nanophotonics (OMN), 2011, pp. 33–34.
- [35] K. Janschek, R. Schroedter, T. Sandner, Flatness-based open loop command tracking for quasistatic microscanners, in: ASME Dynamic Systems and Control Conference (DSCC), no. DSCC2013-3865 in Vol. 3, 2013, pp. V003T37A001, 5 pages.
- [36] T. Sandner, T. Grasshoff, M. Schwarzenberg, H. Schenk, Quasistatic microscanner with linearized scanning for an adaptive 3D-laser camera, in: International Conference on Optical MEMS and Nanophotonics (OMN), 2013, pp. 103–104.
- [37] R. Schroedter, M. Roth, T. Sandner, K. Janschek, Modellgestützte flachheitsbasierte Folgeregelung von quasistatischen Mikroskannern (Model- and flatness-based tracking control for quasistatic microscanners), in: Tagungsband Fachtagung Mechatronik, Dortmund, 2015, pp. 25–30.
- [38] K. Janschek, T. Sandner, R. Schroedter, M. Roth, Adaptive Prefilter Design for Control of Quasistatic Microscanners, in: J. Bingfeng (Ed.), Proc. of 6th IFAC Symposium on Mechatronic Systems, Vol. 46, 2013, pp. 197–206.
- [39] R. Schroedter, M. Roth, T. Sandner, K. Janschek, Modellgestützte Bewegungsführung von quasistatischen Mikroskannern (Model-based motion tracking for quasistatic microscanners), in: Tagungsband Fachtagung Mechatronik, Aachen, 2013, pp. 141–146.
- [40] R. Schroedter, K. Janschek, T. Sandner, Jerk and Current Limited Flatness-based Open Loop Control of Foveation Scanning Electrostatic Micromirrors, in: International Federation of Automation and Control (IFAC) Conference, 2014, pp. 2685–2690.
- [41] M. Fliess, L. J., M. P., P. Rouchon, On differentially flat nonlinear systems, in: M. Fliess (Ed.), Nonlinear Control System Design, Pergamon Press, 1992, pp. 408–412.
- [42] M. Fliess, J. Lévine, P. Martin, P. Rouchon, Flatness and defect of non-linear systems: introductory theory and examples, International Journal of Control 61 (6) (1995) 1327–1361.
- [43] A. Isidori, Nonlinear control systems, Springer London, 1995.
- [44] G. Rigatos, G. Zhu, H. Yousef, A. Boulkroune, Flatness-based adaptive fuzzy control of electrostatically actuated MEMS using output feedback, Fuzzy Sets and Systems 290 (2016) 138–157.
- [45] C. G. Agudelo, G. Zhu, M. Packirisamy, L. Saydy, Flatness-based control of an electrostatic torsional micro-mirror with voltage feedback, in: 50th Midwest Symposium on Circuits and Systems, 2007, pp. 654–657.
- [46] G. Zhu, J. Levine, L. Praly, On the differential flatness and control of electrostatically actuated MEMS, in: Proc. of the American Control Conference, 2005, pp. 2493–2498 vol. 4.
- [47] D. H. S. Maithripala, J. M. Berg, W. P. Dayawansa, Nonlinear dynamic output feedback stabilization of electrostatically actuated MEMS, in: Proc. of 42nd IEEE Conference on Decision and Control, Vol. 1, 2003, pp. 61–66 Vol.1.
- [48] D. H. S. Maithripala, B. D. Kawade, J. M. Berg, W. P. Dayawansa, A general modelling and control framework for electrostatically actuated mechanical systems, International Journal of Robust and Nonlinear Control 15 (16) (2005) 839–857.
- [49] T. Sandner, T. Grasshoff, M. Schwarzenberg, R. Schroedter, H. Schenk, Quasistatic microscanner with linearized scanning for an adaptive three-dimensional laser camera, Journal of Micro/Nanolithography, MEMS, and MOEMS 13 (1) (2014) 011114.
- [50] J. T. Thielemann, T. Sandner, S. Schwarzer, U. Cupcic, H. Schumann-Olsen, T. Kirkhus, Tacao: a three-dimensional camera with object detection and foveation, in: SAB Workshops, Vol. 28, 2010, eC FP7 grant no 248623.
- [51] J. T. Thielemann, A. Berge, . Skotheim, T. Kirkhus, Fast high resolution 3d laser scanning by real-time object tracking and segmentation, in: IEEE/RSJ International Conference on Intelligent Robots and Systems, 2012, pp. 3899–3906.
- [52] B. Satzer, C. Baulig, T. Sandner, S. Schwarzer, Micromirror-based sending and detection optical assembly for time-of-flight laser scanners, in: Proc. SPIE 8439, Optical Sensing and Detection II, Vol. 8439, 2012, pp. 84390Z–84390Z–10.
- [53] T. Klose, D. Kunze, T. Sandner, H. Schenk, H. Lakner, A. Schneider, P. Schneider, Stress optimization of a micromechanical torsional spring, in: Nanotechnology (Ed.), Techn. Proc. of the NSTI Nanotechnology Conference, Vol. 3, 2005, pp. 602–605.
- [54] T. Sandner, T. Grasshoff, T. Klose, H. Schenk, J. Massieu, MEMS based Laser Imager with Diagonal Progressive Scanning, in: IEEE 22nd International Conference on Micro Electro Mechanical Systems, 2009, pp. 951–954.
- [55] T. Sandner, H. Conrad, T. Klose, H. Schenk, Integrated Piezoresistive Positionsensor for Microscanning Mirrors, in: W. P. Harald Schenk (Ed.), IEEE/LEOS International Conference on Optical MEMS and Nanophotonics, 2007, pp. 195–196.
- [56] J. Grahmann, H. Conrad, T. Sandner, T. Klose, H. Schenk, Integrated position sensing for 2D microscanning mirrors using the SOI device layer as the piezoresistive mechanical-elastic transformer, in: Proc. of SPIE, MOEMS and Miniaturized Systems VIII, Vol. 7208, 2009, pp. 720808–720808–10.
- [57] R. Schroedter, T. Sandner, K. Janschek, M. Roth, C. Hruschka, Real-time closed-loop control for micro mirrors with quasistatic comb drives, in: W. Piyawattanametha, Y.-H. Park (Eds.), Proc. of SPIE, MOEMS and Miniaturized Systems XV, Vol. 9760, 2016, pp. 976009–976009–13.
- [58] J. Grahmann, A. Dreyhaupt, C. Drabe, R. Schroedter, J. Kamenz, T. Sandner, MEMS-mirror based trajectory resolution and precision enabled by two different piezoresistive sensor technologies, in: W. Piyawattanametha, Y.-H. Park (Eds.), Proc. of SPIE, MOEMS and Miniaturized Systems XV, Vol. 9760, 2016, pp. 976006–976006–11.
- [59] U. Krishnamoorthy, S. Lee, O. Solgaard, Self-aligned vertical electrostatic combdrives for micromirror actuation, Journal of Microelectromechanical Systems 12 (4) (2003) 458–464.
- [60] R. Conant, Micromachined Mirrors, Microsystems Series, Springer, 2003.
- [61] D. Jung, D. Kallweit, T. Sandner, H. Conrad, H. Schenk, H. Lakner, Fabrication of 3D comb drive microscanners by mechanically induced permanent displacement, in: W. P. David L. Dickensheets, Harald Schenk (Ed.), Proc. of SPIE, MOEMS and Miniaturized Systems VIII, Vol. 7208, 2009, pp. 72080A–72080A–11.
- [62] E. T. Carlen, K.-H. Heng, S. Bakshi, A. Pareek, C. H. Mas-trangelo, High-aspect ratio vertical comb-drive actuator with small self-aligned finger gaps, Journal of Microelectromechanical Systems 14 (5) (2005) 1144–1155.
- [63] Y. Li, D. Psychogiou, S. Kühne, J. Hesselbarth, C. Hafner, C. Hierold, Large stroke staggered vertical comb-drive actuator for the application of a millimeter-wave tunable phase shifter, Journal of Microelectromechanical Systems 22 (4) (2013) 962–975.
- [64] D. Jung, T. Klose, T. Grasshoff, T. Sandner, H. Schenk, H. Lakner, 3D hybrid capacitance model for angular vertical comb drives, in: Electronics System-Integration Technology (ESTC) Conference, 2008, pp. 541–546.
- [65] K. Janschek, Mechatronic Systems Design - Methods, Models, Concepts, Springer, 2012.
- [66] R. M. Rosenberg, Analytical dynamics of discrete systems, Math. Concepts Methods Sci. Eng., Plenum, New York, NY, 1977.
- [67] T. Klose, H. Conrad, T. Sandner, H. Schenk, Fluidmechanical damping analysis of resonant micromirrors with out-of-plane comb drive, in: Proc. COMSOL Conference, Hannover, 2008, p. 7 ff.
- [68] T. Klose, Modellierung und entwurf von resonanten mikroak-toren mit elektrostatischem antrieb, Ph.D. thesis, Technischen Universität Dresden, Fakultät für Elektrotechnik und Informationstechnik (2007).
- [69] A. Caspani, C. Comi, A. Corigliano, G. Langfelder, V. Zega, S. Zerbini, Dynamic nonlinear behavior of torsional resonators in MEMS, Journal of Micromechanics and Microengineering 24 (9) (2014) 095025.
- [70] I. Kovacic, M. Brennan, The Duffing Equation: Nonlinear Oscillators and their Behaviour, John Wiley & Sons, Ltd, 2011.
- [71] H. Unbehauen, Regelungstechnik I, Vieweg+Teubner Verlag,

- 2008.
- [72] M. Roth, Ein Beitrag zur Regelung von quasistatischen Mikroskannern zur hochdynamischen und präzisen Strahlpositionierung (Contribution to the feedback control of quasi-static micro scanner for high dynamic and precise beam steering), Master's thesis, Technische Universität Dresden (2013).
  - [73] J. Levine, Analysis and Control of Nonlinear Systems: A Flatness-based Approach, Mathematical Engineering, Springer Berlin Heidelberg, 2009.
  - [74] J. Adamy, Nichtlineare Systeme und Regelungen 2, Springer-Verlag, Berlin Heidelberg, 2014.
  - [75] V. Hagenmeyer, E. Delaleau, Exact feedforward linearization based on differential flatness, International Journal of Control 76 (6) (2003) 537–556.
  - [76] V. Hagenmeyer, E. Delaleau, Robustness analysis of exact feedforward linearization based on differential flatness, Automatica 39 (11) (2003) 1941–1946.
  - [77] M. Fliess, C. Join, Model-free control, International Journal of Control 86 (12) (2013) 2228–2252.
  - [78] K. Röbenack, Extended Luenberger Observer for Nonuniformly Observable Nonlinear Systems, in: T. Meurer, K. Graichen, E. D. Gilles (Eds.), Control and Observer Design for Nonlinear Finite and Infinite Dimensional Systems, Vol. 322 of Lecture Notes in Control and Information Science, Springer Berlin Heidelberg, 2006, pp. 19–34.
  - [79] A. J. Krener, A. Isidori, Linearization by output injection and nonlinear observers, Systems and Control Letters 3 (1) (1983) 47 – 52.
  - [80] D. Luenberger, Observing the State of a Linear System, IEEE Transactions on Military Electronics 8 (2) (1964) 74–80.
  - [81] K. Röbenack, Computation of the observer gain for extended Luenberger observers using automatic differentiation, IMA Journal of Mathematical Control and Information 21 (1) (2004) 33–47.
  - [82] M. Tomizuka, T.-C. Tsao, K.-K. Chew, Analysis and synthesis of discrete-time repetitive controllers, Journal of Dynamic Systems, Measurement, and Control 111 (3) (1989) 353–358.
  - [83] Y. Chen, C. Wen, Iterative Learning Control: Convergence, Robustness and Applications, Springer, London, UK, 1999.
  - [84] H.-S. Ahn, K. L. Moore, Y. Chen, Iterative learning control: robustness and monotonic convergence for interval systems, Springer, London, UK, 2007.



**Dipl.-Ing. Richard Schroedter** graduated with “Diploma” in Mechatronics in 2013 at Technische Universität Dresden and got the best paper award at “VDI Mechatronik Fachtagung” in the same year. He is now PhD student at Fraunhofer Institute for Photonic Microsystems researching on the control of electrostatic micro mirrors.



**Dipl.-Ing. Matthias Roth** studied Mechatronics at Technische Universität Dresden and got the prize for his best “Diploma” thesis in mechatronics in 2014. He is now PhD student at Institute of Automation at the Faculty of Electrical and Computer Engineering at Technische Universität Dresden with focus on spatial beam shaping.



Following his “Dr.techn.” degree at Technische Universität Graz (Austria), **Prof. Dr. techn. Klaus Janschek** worked several years in industry in the field of research and development for servohydraulic and satellite systems. Since 1995 he is Professor for Automation Engineering and Managing Director Institute of Automation at the Faculty of Electrical and Computer Engineering at Technische Universität Dresden (Germany). He was guest professor at several universities and is member of the technical board of International Federation of Automatic Control (IFAC).



**Dr. Thilo Sandner** got the Infineon prize for the best PhD thesis in 2004 in the field of microelectronics at Technische Universität Dresden, Faculty Electrical Engineering. Since 2007 he works at Fraunhofer Institute for Photonic Microsystems in research and development of micro scanning mirrors and MOEMS.